

Direct observations of shock-induced melting in a porous solid using time-resolved x-ray diffractionA. Mandal^{*} and B. J. Jensen*Shock and Detonation Physics, Los Alamos National Laboratory, Los Alamos, New Mexico 87545, USA*M. C. Hudspeth[†] and S. Root*Dynamic Material Properties, Sandia National Laboratories, Albuquerque, New Mexico 87185, USA*

R. S. Crum and M. C. Akin

Physics Division, Lawrence Livermore National Laboratory, Livermore, California 94550, USA

(Received 18 May 2018; accepted 27 May 2020; published 8 June 2020)

In this work we provide direct evidence of shock-induced melting and associated kinetics in a porous solid (aluminum powder) using time-resolved x-ray diffraction. Unambiguous evidence of melting in 50% porous aluminum (Al) powder samples, shocked to peak pressures between ~ 13 -19 GPa, was provided by the broadening of the Debye-Scherrer ring corresponding to the (111) peak. Shocked Al powder did not melt completely in any of our experiments within the durations of measurement. Incomplete (partial) melting of the powder, even after several hundreds of nanoseconds of shock loading, provides insights into thermal transport with Al powder particles under high-pressure dynamic loading. Such insights are quite valuable for developing well-constrained melting models and thermodynamic equations of state for porous Al and other porous solids relevant to planetary and materials science.

DOI: [10.1103/PhysRevMaterials.4.063604](https://doi.org/10.1103/PhysRevMaterials.4.063604)**I. INTRODUCTION**

Melting is a key first order solid-to-liquid phase transition that affects the equation of state (EOS) of materials [1]. Melting of porous solids (regolith, rock, ice, etc.) as a result of shock wave compression and subsequent release from high pressure during impact cratering and collisions between planetesimals is widespread in the solar system [2–4]. Accurate knowledge of the conditions required for incipient (intergranular) and bulk melting in shocked porous solids, as well as the associated kinetics, are crucial for simulating and understanding phenomena important to planetary science. Examples of such phenomena include post-impact thermal evolution in planetesimals [4], crater and chondrule formation [5,6], formation of melt pockets and entrapment of atmospheric gases within them [7], and hazard mitigation by asteroid deflection [8]. Understanding shock-induced melting of porous solids is also important for gaining better control over shock consolidation [9] and shock synthesis [10] processes important to materials scientists.

In the past, melting of porous solids under shock loading has been inferred from a change in the measured pressure-density Hugoniot slope [2,11], luminescence, viscosity, sound speed, or electrical conductivity in the shocked state [12–15]. For example, Asay and Hayes [12] estimated that incipient melting takes place at ~ 7 GPa and completes at around

14 GPa in 40% porous Al (1.6 g/cm^3) by measuring sound speed through shocked samples. However, these measurements only provide indirect evidence of melting and lacked insight into the underlying kinetics.

In this work our objective is to directly examine shock-induced melting and associated melt kinetics in porous aluminum (Al) using time-resolved synchrotron x-ray diffraction (XRD) coupled with a dynamic loading platform (powder gun). Aluminum is our material of choice for a few reasons: (a) it is adequately x-ray transparent, (b) previous shock-induced melt studies on porous Al [12,14] could be used to guide the pressure range examined in our study, (c) its high-pressure response is well studied [16–20], and (d) high pressure-high temperature thermodynamic properties are well known [21–23]. In our work, 50% porous Al powder samples were shock loaded to peak pressures of ~ 13 -19 GPa, and the ensuing melt kinetics was examined directly by recording four diffraction images of the shocked Al powder separated by 153.4 ns and observing the evolution of Debye-Scherrer rings.

II. EXPERIMENTAL DETAILS

Plate-impact experiments, coupled with dynamic XRD, were conducted at the Dynamic Compression Sector (DCS) of the Advanced Photon Source (APS) to examine shock-induced melting of 48.5(± 0.1)% porous Al powder. Aluminum powder was purchased from Atlantic Equipment Engineers, a division of Micron Metals, Inc. The nominal purity of the powder and the particle size were quoted as 99.9% and -325 mesh ($< 45 \mu\text{m}$), respectively. As shown

^{*}anirban_mandal@lanl.gov[†]Present Address: XTD-NTA, Los Alamos National Laboratory, Los Alamos, NM 87545, USA.

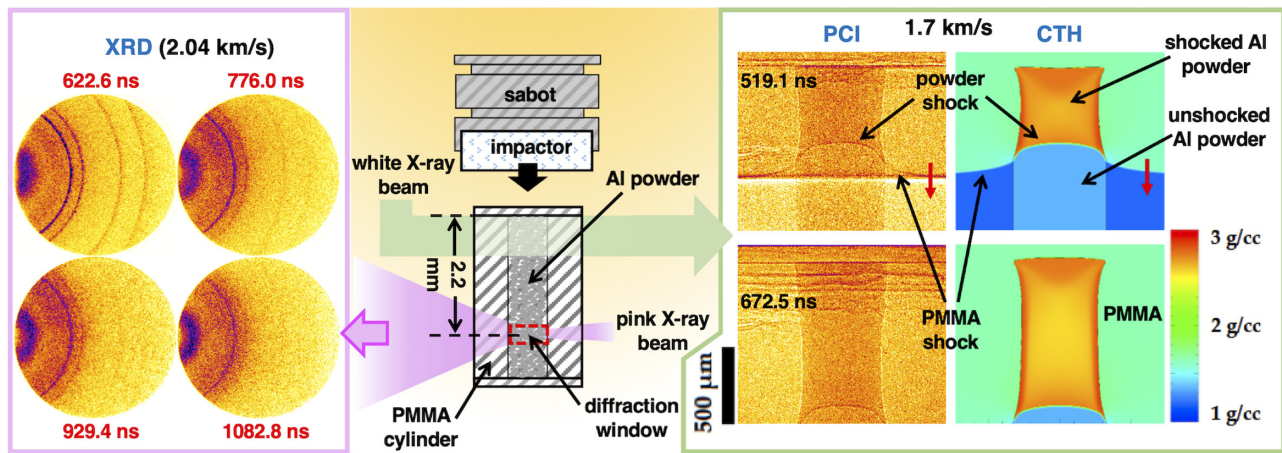


FIG. 1. Schematic of the overall configuration used in the x-ray diffraction (XRD) and x-ray phase-contrast imaging (PCI) experiments conducted separately to examine shock-induced melting of Al powder is shown in the middle. The 0.8-mm-diameter powder column was encapsulated in a PMMA cylinder using PMMA baseplates. Examples of (left) XRD and (right) PCI data are shown in false color, along with CTH simulations of the PCI data. Time is relative to impact.

in Fig. 1, targets for dynamic XRD experiments contained a 800- μm -diameter Al powder column encapsulated in a 8-mm-diameter \times 6.7-mm-long PMMA cylinder. The powder was contained by epoxying \sim 0.7-mm-thick PMMA baseplates on either side of the PMMA cylinder. The powder targets were impacted by $\langle 100 \rangle$ -oriented lithium fluoride (LiF) impactors at 1.63, 2.04, and 2.42 km/s. The 10-mm-diameter \times 4-mm-thick LiF impactors, mounted on polycarbonate projectiles, were launched using a 12.7-mm-bore powder gun. Projectile velocities were measured with 0.5% uncertainty using a laser interruption system attached to the gun muzzle.

Following impact, a planar shock wave propagated through the PMMA baseplate, which subsequently interacted with the PMMA/Al powder interface and resulted in transmitted shock waves in the powder and the surrounding PMMA. X-ray phase contrast images (PCI), obtained from a separate set of experiments [24] conducted at DCS, and corresponding CTH hydrocode [25] simulations are presented in Fig. 1 to help visualize the propagating shock waves and resulting deformation of the powder column. The continuum-scale CTH simulations, validated by the PCI data, provided the thermomechanical states of the shock-compressed powder required for the XRD data analysis presented later. Details of CTH simulations and PCI experiments [26] are provided in the Appendix and Supplemental Material [27], respectively.

X-ray diffraction measurements of the shocked Al powder were made using the standard 24-bunch mode of the APS storage ring, which consists of 80 ps FWHM x-ray bunches separated by 153.4 ns. The spectral flux profile of each x-ray bunch had an asymmetric shape with a peak near 23.1 keV ($\Delta E/E \approx 2\%$). As shown in Fig. 1, XRD experiments were carried out in the transmission geometry where the incident x-ray beam was perpendicular to the gun axis and the PMMA cylinder. The incident beam was focused on the Al powder between 2.11 and 2.36 mm away from the impact face of the powder column. The 300 (W) \times 800 (H) μm^2 focal spot, referred to as the “diffraction window,” is indicated in Fig. 1; window width (W) is defined along the cylinder axis. In each experiment, four diffraction images of the shocked powder

were recorded using the DCS diffraction detector system [28]. The x-ray detector has a 75-mm-diameter active area. Its modular front end consists of an x-ray phosphor ($\text{Lu}_2\text{SiO}_5 : \text{Ce}$, LSO)-coated fiber optic plate that converts incident x-ray photons to visible light, a fiber optic taper, and a microchannel plate (MCP) image intensifier. The back end of the detector system includes beamsplitters, four camera lenses, and four PI-MAX@4 intensified charge-coupled device (ICCD) cameras. Each ICCD camera was gated sequentially to capture an exposure from a single x-ray bunch; thus, four detectors allowed recording of four diffraction patterns that are 153.4 ns apart in time. For additional details, see the Supplemental Material [27].

III. DATA REDUCTION AND RESULTS

Representative diffraction images, from the 2.04 km/s experiment, are shown on the left of Fig. 1. Raw diffraction images from all three experiments, as well as representative ambient diffraction images taken prior to conducting these experiments, are provided in the Supplemental Material [27]. Despite short decay lifetimes of the LSO phosphor coating on the fiber optic plate and the P47 phosphor anode in the MCP image intensifier of the DCS detector system, after-image contributions resulting from residual phosphor decays of preceding x-ray bunches are unavoidable in the 24-bunch mode. After-image contributions were subtracted from the raw diffraction images following the method described in Ref. [28]. The after-image corrected diffraction patterns were then integrated azimuthally in HiSPoD [29] to produce XRD line profiles. Finally, PMMA background was subtracted from the integrated line profiles as described in Ref. [27].

Temporal evolutions of the background-subtracted line profiles corresponding to experiments conducted at impact velocities of 1.63, 2.04, and 2.42 km/s are shown in Figs. 2(a)–2(c), respectively. The corresponding powder peak pressures were estimated to be about 13.0, 15.8, and 18.8 GPa, respectively, from CTH simulations. Peak pressures were realized along the center of the powder column at the propagating

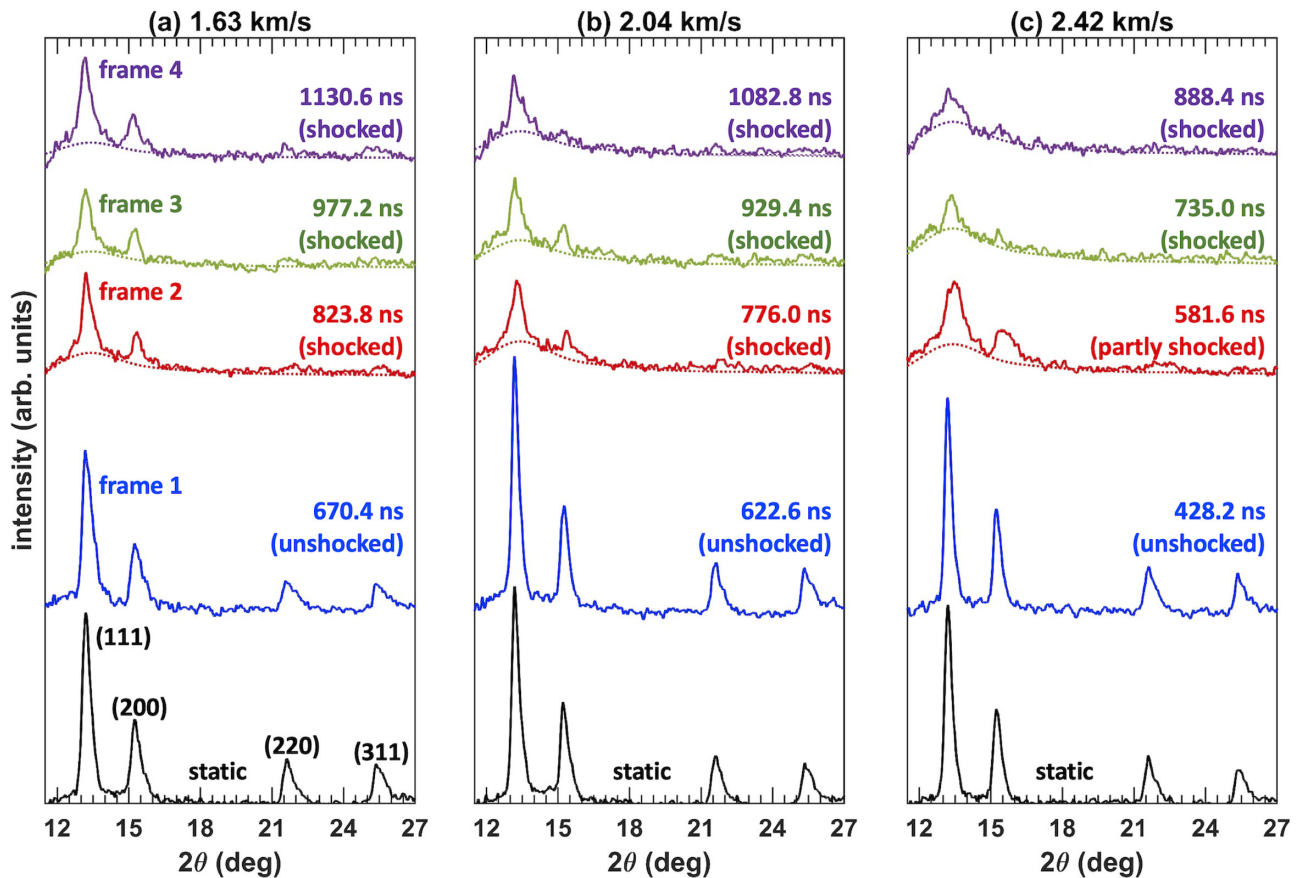


FIG. 2. Temporal evolutions of the $\sim 50\%$ porous Al powder diffraction line profiles, background subtracted and adjusted for differences in detector sensitivities, obtained from experiments conducted at impact velocities of (a) 1.63, (b) 2.04, and (c) 2.42 km/s are shown with solid lines. The dotted lines in frames 2–4 show the corresponding liquid diffuse background, which is indicative of melting. The powder shock had propagated partway into the diffraction window in frame 2 of the 2.42 km/s experiment, resulting in partly shocked powder within the diffraction window and a relatively broadened diffraction line profile. Time is relative to impact.

shock front, which was followed by a release in pressure. Static data recorded prior to conducting each dynamic experiment are shown with the black lines; the (111), (200), (220), and (311) peaks of Al powder (face-centered cubic $Fm\bar{3}m$) are indicated in Fig. 2(a). The corresponding diffraction profiles recorded 153.4 ns apart during the dynamic event are shown with blue (frame 1), red (frame 2), green (frame 3), and purple (frame 4) solid lines. Powder volumes probed in subsequent dynamic frames of an experiment are different due to the flow of shock-compressed powder particles through the diffraction window, which is fixed in space, in the direction of the propagating powder shock. In all experiments, frame 1 images were recorded prior to the arrival of the powder shock at the diffraction window. Measured peak intensities (integrated intensity) in frames 2–4 of all listed experiments correspond to shock compressed powder, and they are lower than the corresponding unshocked (frame 1) intensities.

Broadening of the (111) peak in frames 2–4 and the presence of a diffuse background or “hump” underneath it, observed in both the raw 2D images (see Fig. 1 and Ref. [27]) and the integrated line profiles (Fig. 2), provide unambiguous evidence of melting of the shock-compressed Al powder in all three experiments. Similar evidence was provided in support of melting in previous shock [30,31] and static high-pressure

[32,33] experiments. Liquid diffuse background contributions to the measured line profiles in frames 2–4 are shown in Figs. 2(a)–2(c) with the dotted lines; construction of the liquid diffuse background is described in Ref. [27].

Liquid diffuse background subtracted line profiles, presented in Figs. 3(a)–3(c), show that the largest peak intensity loss occurred in the 2.42 km/s experiment. At least a part of the peak intensity loss observed in all three experiments was due to shock-induced melting of the powder. Since complete melting of the powder would have led to complete loss of all peak intensities [34], Figs. 3(a)–3(c) suggest that the shocked powder did not melt completely within the duration of our measurements. In the following, we attempt to determine the melt fraction within the shocked Al powder by analyzing the observed (111) peak intensity loss. We begin by identifying and accounting for all possible contributions toward the observed peak intensity loss.

IV. PEAK INTENSITY LOSS FROM CHANGE IN POWDER DENSITY AND TEMPERATURE

Changes in Al powder and PMMA densities following shock compression, along with change in the shock-compressed powder temperature, are primarily responsible for

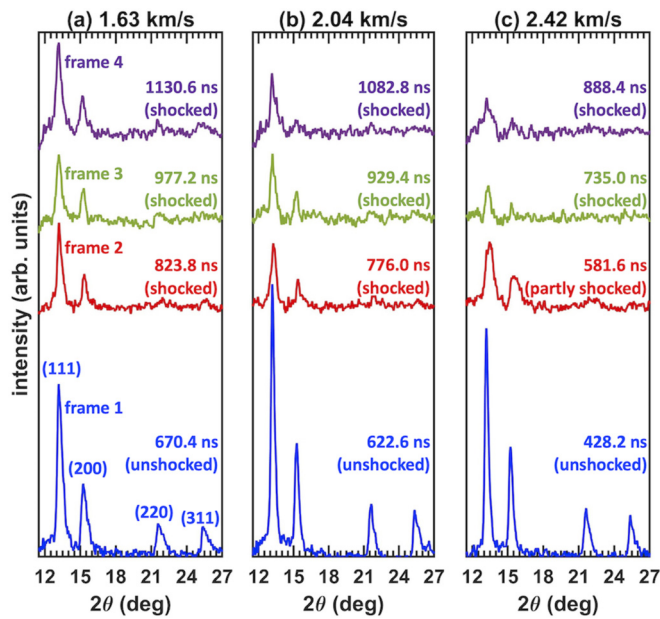


FIG. 3. Temporal evolution of (111) peak intensities in shock compressed Al powder in all three experiments after subtracting liquid diffuse backgrounds from the diffraction line profiles presented in Figs. 2(a)–2(c). Time is relative to impact.

the observed differences between the shocked and unshocked (or ambient) peak intensities measured in a given experiment. While texture evolution can also lead to peak intensity loss, recorded Debye-Scherrer images do not indicate any significant change in the powder texture following shock compression (see Ref. [27]).

To decouple the contributions from changes in the density and temperature toward the observed peak intensity drop, we begin by estimating the integrated (111) peak intensities (I_{111}^{es}) that would have resulted in frames 2–4 solely from the density changes in the shocked powder and the PMMA container. Below, we describe the procedure that was adopted, following Ref. [35], to estimate the value of I_{111}^{es} in a given diffraction frame using the corresponding static (111) peak intensity and the CTH-calculated densities of shock compressed Al powder and PMMA within the diffraction window.

We begin by showing a cross section of the PMMA cell containing the Al powder column in Fig. 4, where the size of the powder column is exaggerated for clarity. The shaded rectangle represents a diffracting element within the powder that contributes to the measured peak intensities in our experiments. The parallelepiped diffracting element has a thickness W equal to the width (300 μm) of the incident x-ray beam along the length of the powder column. Therefore, the volume of the diffracting element is $dV = dx \times dy \times W$. The cylindrical diffracting powder volume with a diameter equal to the powder column diameter (800 μm) and length equal to W is then made up of numerous such parallelepiped diffracting elements that contribute to the overall scattered x-ray intensity measured in each diffraction image. The PMMA cylinder was also assumed to be made up of similar parallelepipeds,

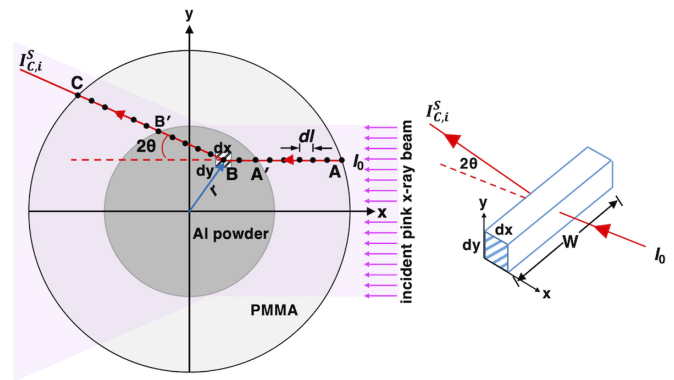


FIG. 4. Schematic of the PMMA cylinder cross section showing the parallelepiped diffracting element (i th element) within the Al powder column is presented on the left. A side view of the diffracting element is shown on the right.

which absorb the incident intensity but do not contribute to the scattered intensity.

In reality, densities of the shocked powder and PMMA within the “diffraction window” depends on both the location along the cylinder axis (z) and radius (r). This is illustrated through density snapshots presented in Fig. 5, where CTH-calculated Al powder densities at two different radial locations are shown. The density of the shocked powder (and PMMA) at a given r location within the diffraction window does not vary significantly with z location (axial position), unless the shock is within the window. Therefore, to simplify our analysis, we assumed that densities of Al powder (ρ^{Alp}) and PMMA (ρ^{PMMA}) within the diffraction window is only a function of r , i.e., density of the parallelepiped diffracting element depends on its distance r from the center of the PMMA cylinder. The density of each parallelepiped element was taken to be the

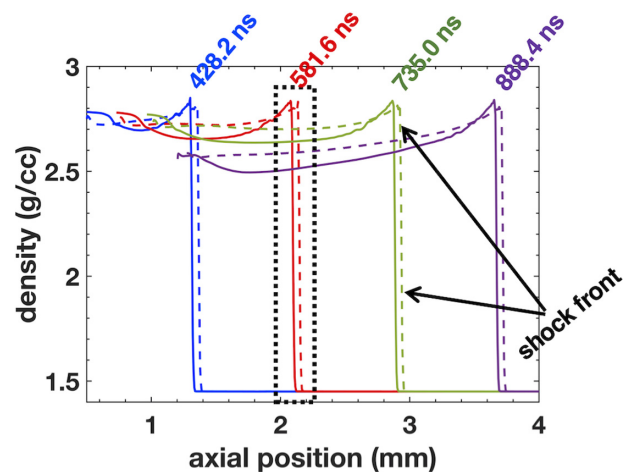


FIG. 5. CTH-calculated densities in the 2.42 km/s experiment along the center of the powder column ($r = 0$ mm) and along the horizontal powder/PMMA interface ($r = 0.4$ mm) are shown with solid and dashed lines, respectively. The blue, red, green, and purple lines represent density snapshots at the time of recording frames 1–4, respectively. The diffraction window is indicated by the dotted rectangle. Time is relative to impact.

average of all density values along its length W . An exception to this was only seen in frame 2 of Fig. 5.

Now consider incident x rays that impinged on the i th diffraction element, located at B in Fig. 4, at a distance r from the center of the PMMA cylinder along the path $AA'B$, and were subsequently scattered at an angle 2θ along $BB'C$. The incident intensity I_0 was partially attenuated at point B due to absorption according to

$$I_{B,i} = I_0 e^{-\left(\mu_m^{\text{PMMA}} \int_A^{A'} \rho^{\text{PMMA}}(r) dl + \mu_m^{\text{Al}} \int_{A'}^B \rho^{\text{Alp}}(r) dl\right)_i}. \quad (1)$$

In Eq. (1), μ_m^{PMMA} and μ_m^{Al} are mass absorption coefficients of PMMA and Al powder, respectively. Through interpolation, values of μ_m^{PMMA} and μ_m^{Al} at 23.1 keV were calculated to be 0.4883 and 2.724 cm²/g, respectively, from μ_m values listed on the NIST website [36]. Densities of PMMA and Al powder are constants, i.e., $\rho^{\text{PMMA}} = 1.186$ g/cc and $\rho^{\text{Alp}} = 1.39$ g/cc under ambient conditions. For shock-compressed PMMA and Al powder, $\rho^{\text{PMMA}}(r)$ and $\rho^{\text{Alp}}(r)$ values were obtained from CTH-calculated densities as described above.

Now, intensity of x rays scattered by the i th diffracting element at B is given by

$$\begin{aligned} I_{B,i}^S &= I_{B,i} K \frac{\psi_i}{v_i^2} \\ &= I_0 K \frac{\psi_i}{v_i^2} e^{-\left(\mu_m^{\text{PMMA}} \int_A^{A'} \rho^{\text{PMMA}}(r) dl + \mu_m^{\text{Al}} \int_{A'}^B \rho^{\text{Alp}}(r) dl\right)_i}, \end{aligned} \quad (2)$$

where K is a constant which contains the structure factor, Lorentz-polarization factor, multiplicity, and other constants, v_i is the unit cell volume of Al, and ψ_i is the solid volume fraction of Al within the i th diffracting element [35,37]. For powder density of $\rho^{\text{Alp}}(r) < \rho_0^{\text{Al}}$, $\psi_i = \rho^{\text{Alp}}(r)/\rho_0^{\text{Al}}$ and $v_i = v_0$, where $\rho_0^{\text{Al}} = 2.703$ g/cc is the density of solid Al and v_0 is the unit cell volume of Al under ambient conditions. For $\rho^{\text{Alp}}(r) \geq \rho_0^{\text{Al}}$, $\phi_i = 1$ and $v_i = v_0[\rho_0^{\text{Al}}/\rho^{\text{Alp}}(r)]$.

The intensity of the x rays scattered by i th diffracting element at B gets further attenuated while propagating through Al powder and PMMA along $BB'C$. Therefore, the scattered intensity at point C is

$$I_{C,i}^S = I_{B,i}^S e^{-\left(\mu_m^{\text{PMMA}} \int_B^C \rho^{\text{PMMA}}(r) dl + \mu_m^{\text{Al}} \int_B^{B'} \rho^{\text{Alp}}(r) dl\right)_i}. \quad (3)$$

Equation (3) can be rewritten as

$$I_{C,i}^S = I_0 K \frac{\psi_i}{v_i^2} e^{-\left(\mu_m^{\text{PMMA}} \chi_i^{\text{PMMA}} + \mu_m^{\text{Al}} \chi_i^{\text{Alp}}\right)}, \quad (4)$$

where $\chi_i^{\text{PMMA}} = \int_A^{A'} \rho^{\text{PMMA}}(r) dl + \int_B^C \rho^{\text{PMMA}}(r) dl$ and $\chi_i^{\text{Alp}} = \int_{A'}^{B'} \rho^{\text{Alp}}(r) dl$ are total mass thicknesses of PMMA and Al powder layers, respectively, that the incident x rays scattered by the i th diffracting element go through. Here mass thickness χ is defined as $\chi = \int \rho dl$.

For ambient or preshot measurements, Eq. (4) becomes

$$I_{C,i}^{S,\text{amb}} \approx I_0 K \left(\frac{0.51}{v_0^2}\right) e^{-\left(0.58L_i^{\text{PMMA}} + 3.79L_i^{\text{Alp}}\right)}, \quad (5)$$

where L_i^{PMMA} and L_i^{Alp} are total thicknesses of the PMMA and Al powder, respectively, that incident x rays scattered by the i th diffracting element go through.

Total intensity of all x rays scattered by the Al powder within the diffraction window in the dynamic experiments is obtained by summing the contribution from each diffracting element and it is given by

$$\begin{aligned} I_{\text{total}}^S &= \sum_{i=1}^N I_{C,i}^S \\ &= I_0 K \sum_{i=1}^N \frac{\psi_i}{v_i^2} e^{-\left(\mu_m^{\text{PMMA}} \chi_i^{\text{PMMA}} + \mu_m^{\text{Al}} \chi_i^{\text{Alp}}\right)}, \end{aligned} \quad (6)$$

where N is the total number of diffracting elements within the diffraction powder volume, i.e., diffraction window. For preshot (ambient) measurement,

$$\begin{aligned} I_{\text{total}}^{S,\text{amb}} &= \sum_{i=1}^N I_{C,i}^{S,\text{amb}} \\ &\approx I_0 K \left(\frac{0.51}{v_0^2}\right) \sum_{i=1}^N e^{-\left(0.58L_i^{\text{PMMA}} + 3.79L_i^{\text{Alp}}\right)}. \end{aligned} \quad (7)$$

Since $I_{\text{total}}^{S,\text{amb}} = I_{111}^{\text{amb}}$ and $I_{\text{total}}^{S,\text{dyn}} = I_{111}^{\text{es}}$ when $2\theta = 13.2^\circ$, estimated (111) peak intensity I_{111}^{es} was calculated from the following equation using $2\theta = 13.2^\circ$:

$$\frac{I_{111}^{\text{es}}}{I_{111}^{\text{amb}}} = \frac{\sum_{i=1}^N \frac{\psi_i}{v_i^2} e^{-\left(\mu_m^{\text{PMMA}} \chi_i^{\text{PMMA}} + \mu_m^{\text{Al}} \chi_i^{\text{Alp}}\right)}}{\left(\frac{0.51}{v_0^2}\right) \sum_{i=1}^N e^{-\left(0.58L_i^{\text{PMMA}} + 3.79L_i^{\text{Alp}}\right)}}. \quad (8)$$

The ambient (111) peak intensity I_{111}^{amb} is calculated from the preshot diffraction images recorded prior to conducting each dynamic experiment. Once I_{111}^{amb} is known, I_{111}^{es} can be calculated from Eq. (8), which provides a reasonable quantitative estimate.

In Fig. 6(a) we plot the relative magnitudes of the measured (I_{111}^m) and the corresponding estimated (I_{111}^{es}) intensities of the (111) peak against the ‘‘shocked duration’’ of the corresponding diffracting powder volumes in frames 2–4 of all four experiments. As shown in Fig. 6(b), shocked duration provides a measure of the time duration for which a powder volume was under compressive loading before arriving at the diffraction window; its value was determined from the CTH-calculated loading history of the powder. The error bars shown in Fig. 6(a) represent the uncertainties in the estimation of relative detector sensitivities and in subtracting the liquid diffuse background from the XRD line profiles shown in Figs. 2(a)–2(c). Since I_{111}^{es} values were calculated by considering only density changes in the shocked powder and PMMA, values of ($I_{111}^m/I_{111}^{\text{es}} < 1$ in Fig. 6(a) are indicative of additional peak intensity loss resulting due to a change in the shocked powder temperature. Both a Debye-Waller (DW) effect [37,38] and melting of powder particles [34] could lead to peak intensity loss caused by a change in the powder temperature in our experiments.

V. DISCUSSION

Pressure (P)-temperature (T) values in the shocked powder volumes located within the diffraction window in frames 2–4 of a given experiment are highlighted by the shaded regions

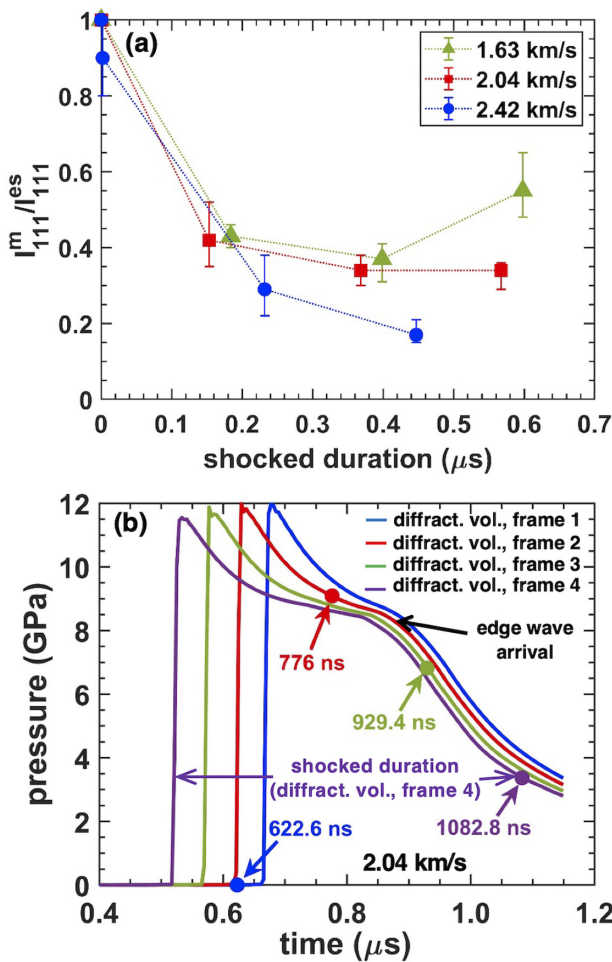


FIG. 6. (a) Measured (111) peak intensities (I_{111}^m), normalized by the corresponding peak intensities (I_{111}^{es}) estimated considering density changes alone, are plotted against the shocked duration (defined in the text) of corresponding diffracting powder volumes in frames 2–4 of all four experiments to illustrate the effect of temperature rise in the shocked powder. (b) CTH-calculated loading histories of the powder particles located at the center of the diffracting powder volumes in frames 1–4 of the 2.04 km/s experiment are shown. Time is relative to impact. The rising points of pressure, which correspond to the instances of being shocked, are different because powder volumes probed in subsequent dynamic frames were different due to flow of the shock-compressed powder through the diffraction window, which was fixed in the laboratory frame. The solid circle on each loading profile indicates the recording time of the corresponding diffraction frame.

within each bounding polygon in Fig. 7. Frame 1 is not included because it was recorded before shock arrival at the diffraction window. These P - T values, which are obtained from continuum-scale CTH simulations, agree quite well with those reported by Asay and Hayes [12] for shock loading of porous Al samples of comparable initial density. While CTH simulations capture the spatial variation in the powder temperature (and pressure) caused by variation in shock strength along the powder shock front and the release wave following the shock, they do not capture particle-scale temperature inhomogeneity existing within shocked porous solids [39]. During shock compaction, the outer layer of each Al powder

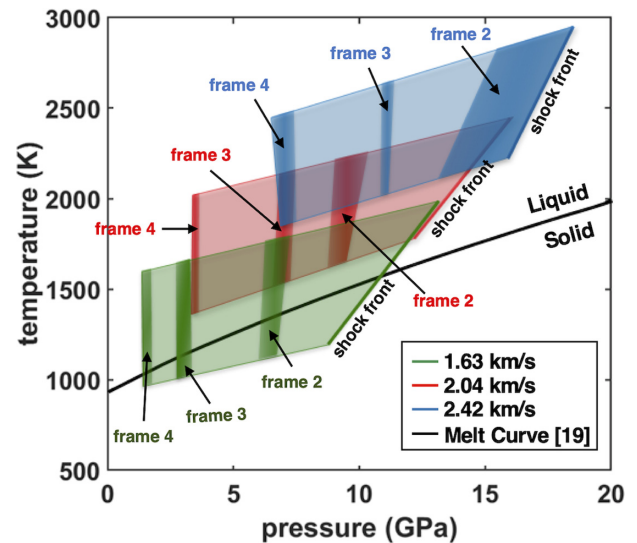


FIG. 7. The four-sided polygons encompass CTH-calculated pressure (P)-temperature (T) states in the shock-compressed diffracting powder volumes in the 1.63, 2.04, and 2.42 km/s experiments. Shaded regions inside each polygon highlight the P - T states within the diffracting powder volume during recording of frames 2–4 of the corresponding experiment.

particle undergoes severe friction and plastic deformation [40]. This leads to formation of localized regions of energy concentration known as “hotspots” on particle boundaries, while the shocked interior remains a much lower temperature [12,41,42]. Subsequent thermal equilibration within each particle is achieved via conductive heat transfer from the hotter boundary to the cooler interior [12,43].

CTH-calculated temperatures shown in Fig. 7 are those that would have resulted in the shocked powder if thermal equilibrium were reached within each powder particle, i.e., aforementioned temperature inhomogeneity within each powder particle were eliminated via heat transfer. In this scenario, Fig. 7 suggests that shock compressed diffracting powder volumes in frames 2–4 of the 2.04 and 2.42 km/s experiments would have melted completely because the corresponding calculated P - T states lie above the Al melt curve. Consequently, all Al peaks would have disappeared from recorded diffraction images [34] corresponding to these frames, except for frame 2 of the 2.42 km/s experiment where the diffracting powder volume is partially shocked. However, this is not consistent with the data presented in Figs. 2, 3, and 6(a), which clearly show that the (111) peak persists, albeit with decreasing intensities, in all diffraction frames corresponding to 2.04 and 2.42 km/s experiments. Even the (200) peak is seen to persist until frame 3 in both of these experiments. Persistence of Al (111) and (200) peaks in our recorded diffraction images strongly suggests that the shock compressed diffracting powder volumes did not melt completely in these experiments.

Incomplete (partial) melting of shocked Al powder in the 2.04 and 2.42 km/s experiments, therefore, indicates that thermal equilibrium was not reached within powder particles in the duration of our measurements. While mechanical equilibrium in the shocked powder is typically reached within tens of nanoseconds, particle-scale thermal equilibrium is not achieved as rapidly [12]. In fact, analysis of our

diffraction data, as presented in Fig. 6(a), shows that thermal equilibration within powder particles was not achieved in the 2.04 and 2.42 km/s experiments even after ~ 600 and 450 ns, respectively, following shock loading. Since the time required to reach particle-scale thermal equilibrium depends on both particle size and thermal diffusivity of the powder material [43,44], insights into thermal transport in porous Al under high-pressure dynamic loading can be gained from our study. Additional insights could be gained by performing similar dynamic x-ray diffraction experiments on porous Al powder with different grain sizes. Such insights are important for the development of well-constrained heat transfer and melting models for Al powder and other porous solids relevant to planetary and materials science.

Although powder particles did not reach thermal equilibrium in our experiments, temperature of the particle interior increased, while temperature of the particle boundaries decreased, toward the CTH-calculated values shown in Fig. 7 with increasing shocked duration due to thermal conduction. Increase in the particle interior temperature close to and beyond the melt temperature likely led to the (111) peak intensity loss with shocked duration seen in Fig. 6(a) in all three experiments. While mesoscale simulations are required to confirm this, an increase in (111) peak intensity in the 1.63 km/s experiment following ~ 400 ns of shocked duration may have resulted from either quenching or due to corresponding P - T states falling below the Al melt curve.

VI. CONCLUSIONS

In this work we provide direct evidence of shock-induced melting and associated kinetics in a porous solid (Al powder) using time-resolved x-ray diffraction. Unambiguous evidence of melting in aluminum (Al) powder samples, shocked to peak pressures between ~ 13 -19 GPa, was provided by the broadening of the Debye-Scherrer ring corresponding to the (111) peak. Furthermore, our diffraction data indicated that the shocked Al powder did not melt completely within the durations of our measurement in all three experiments. Incomplete melting of the shocked powder, when combined with CTH-calculated P - T states, suggested that thermal equilibrium within powder particles was not reached even after ~ 600 and 450 ns, respectively, following shock loading in the 2.04 and 2.42 km/s experiments. Since the time to reach particle-scale thermal equilibration depends on average particle size and thermal diffusivity of the powder, the diffraction data obtained in this work provide insights into the thermal transport process in porous Al under high-pressure dynamic loading. Such insights are needed to develop well-constrained heat transfer and melting models, as well as the development of high-pressure thermodynamic EOS, for shocked Al powder and other porous materials, which will significantly impact dynamic compression problems across multiple fields, including planetary and materials science.

ACKNOWLEDGMENTS

This publication is based upon the work performed by Los Alamos National Laboratory (LANL), Sandia National Laboratories (SNL), and Lawrence Livermore National Laboratory (LLNL) at the Dynamic Compression Sector (DCS)

TABLE I. Equation of state (EOS) parameters for impactor and cylinder/baseplate materials.

Material	EOS	ρ_0 (g/cc)	C_0 (km/s)	s	Γ_0
PMMA	MG	1.186	2.30	1.75	0.91
LiF	MG	2.638	5.15	1.35	1.69
6061 Al	MG	2.703	5.22	1.37	1.97

of the Advanced Photon Source (APS). All PCI data shown here were obtained using LANL's novel multiframe x-ray phase contrast imaging (MPCI) system developed on the IMPULSE (IMPact System for ULtrafast Synchrotron Experiments) capability at APS. Nick Sinclair, Adam Schuman, Drew Rickerson, Brendan Williams, Yuelin Li, and other DCS team members are thanked for their assistance with the XRD and PCI experiments. Nick Sinclair is also thanked for sharing the unpublished manuscript on after-image correction. Chuck Owens and Joe Rivera (LANL) are thanked for sample preparation. Adam Iverson, Carl Carlson, and Matt Teel (National Security Technologies, LLC) are thanked for their help with PCI detectors. Discussions with Tao Sun (Sector-32, APS) are acknowledged. A.M. and B.J.J. acknowledge the financial support from LANL's Science Campaigns, Joint Munitions Program, and MaRIE concept, and National Security Technologies Shock Wave Physics Related Diagnostic programs. LANL is operated by Triad National Security, LLC for the National Nuclear Security Administration (NNSA) of the US Department of Energy (DOE) under Contract No. 89233218CNA000001. M.C.H. and S.R. acknowledge financial support provided by the Truman fellowship (LDRD) and Science Campaigns within SNL. SNL is a multimission Laboratory managed and operated by National Technology and Engineering Solutions of Sandia LLC, a wholly owned subsidiary of Honeywell International Inc., for the US DOE's National Nuclear Security Administration under Contract DE-NA0003525. R.S.C. and M.C.A.'s work was performed under the auspices of the US DOE by LLNL under Contract No. DE-AC52-07NA27344 and was supported by LLNL Laboratory Directed R&D Program (tracking No. 16-ERD-010). The Dynamic Compression Sector is operated by Washington State University under the US DOE/NNSA Award No. DE-NA0003957. This research used resources of the APS, a U.S. DOE Office of Science User Facility operated for the DOE Office of Science by Argonne National Laboratory under Contract No. DE-AC02-06CH11357.

APPENDIX: CTH SIMULATIONS

The multimaterial Eulerian shock wave code CTH [25] was utilized to simulate the 2D, axisymmetric shock evolution for all XRD experiments listed above. CTH hydrocode was also used to simulate additional x-ray PCI experiments performed to image the propagating shock front through the Al powder and subsequent deformation of the powder column. Shock response of LiF $\langle 100 \rangle$ (XRD experiments) and 6061 Al (PCI experiments) impactors and PMMA cylinder/baseplate were modeled using Mie-Grüneisen (MG) EOS. PMMA was additionally assumed to be a linearly elastic, perfectly plastic solid with a yield strength of 50 MPa and a Poisson's ratio

of 0.3. The values of ambient density (ρ_0) bulk sound speed (C_0), slope of the shock velocity–particle velocity curve (s), and Grüneisen parameter (Γ_0) used to describe PMMA, LiF, and 6061 Al response are listed in Table I.

Shock response of the Al powder was modeled using SESAME EOS 3700 [45]. The compaction response of the powder was captured using the well known P - α model [46,47]:

$$\alpha = 1 + (\alpha_E - 1)[(P - P_E)/(P_s - P_E)]^n, \quad (\text{A1})$$

where P is the shock pressure and α is the ratio of specific volumes of the porous material and the corresponding fully dense solid. It was assumed that the elastic regime persists up to a pressure (P_e) of 20 MPa, which is significantly lower than the pressure (P_s) of 100 MPa required for complete void elimination. The scaling parameter (n), which governs the shape of the compaction curve, was set to 2 to match existing 1D shock compaction data on porous Al [16]. For the initial density (ρ_{00}) of the Al powder, a value of 1.45 g/cc was used.

-
- [1] G. E. Duvall and R. A. Graham, *Rev. Mod. Phys.* **49**, 523 (1977).
- [2] S. T. Stewart and T. J. Ahrens, *Geophys. Res. Lett.* **30**, 1332 (2003).
- [3] K. Wünnemann, G. Collins, and G. Osinski, *Earth Planet. Sci. Lett.* **269**, 530 (2008).
- [4] T. M. Davison, F. J. Ciesla, and G. S. Collins, *Geochim. Cosmochim. Acta* **95**, 252 (2012).
- [5] R. G. Kraus, L. E. Senft, and S. T. Stewart, *Icarus* **214**, 724 (2011).
- [6] B. C. Johnson, D. A. Minton, H. J. Melosh, and M. T. Zuber, *Nature (London)* **517**, 339 (2015).
- [7] P. Beck, T. Ferroir, and P. Gillet, *Geophys. Res. Lett.* **34**, L01203 (2007).
- [8] A. Cheng, P. Michel, M. Jutzi, A. Rivkin, A. Stickle, O. Barnouin, C. Ernst, J. Atchison, P. Pravec, and D. Richardson, *Planet. Space Sci.* **121**, 27 (2016).
- [9] W. Gourdin, *Prog. Mater. Sci.* **30**, 39 (1986).
- [10] D. E. Eakins and N. N. Thadhani, *Int. Mater. Rev.* **54**, 181 (2009).
- [11] J. A. Akins, S.-N. Luo, P. D. Asimow, and T. J. Ahrens, *Geophys. Res. Lett.* **31**, L14612 (2004).
- [12] J. R. Asay and D. B. Hayes, *J. Appl. Phys.* **46**, 4789 (1975).
- [13] X.-J. Li, X.-M. Zhou, F.-H. Wang, F.-S. Liu, Z.-Z. Gong, and F.-Q. Jing, *Chin. Phys. Lett.* **18**, 1632 (2001).
- [14] S. D. Gilev, *Combust. Explos. Shock Waves* **41**, 599 (2005).
- [15] P. Song, L.-C. Cai, T.-J. Tao, S. Yuan, H. Chen, J. Huang, X.-W. Zhao, and X.-J. Wang, *J. Appl. Phys.* **120**, 195101 (2016).
- [16] B. M. Butcher, M. M. Carroll, and A. C. Holt, *J. Appl. Phys.* **45**, 3864 (1974).
- [17] D. E. Grady and J. R. Asay, *J. Appl. Phys.* **53**, 7350 (1982).
- [18] R. Boehler and M. Ross, *Earth and Planet. Sci. Lett.* **153**, 223 (1997).
- [19] H. Huang and J. R. Asay, *J. Appl. Phys.* **98**, 033524 (2005).
- [20] J. W. Forbes, *Shock Wave Compression of Condensed Matter* (Springer, New York, 2012).
- [21] B. Sundqvist and G. Bäckström, *Solid State Commun.* **23**, 773 (1977).
- [22] J. E. Jensen, W. A. Tuttle, R. B. Stewart, H. Brechna, and A. G. Prodel, Selected Cryogenic Data Notebook, Technical Report No. BNL 10200-R Brookhaven National Laboratory, Brookhaven, NY, 1980.
- [23] J. E. Hatch (Ed.), *Aluminum: Properties and Physical Metallurgy* (American Society for Metals, Metals Park, Ohio, 1984).
- [24] A. Mandal, M. Hudspeth, B. J. Jensen, and S. Root, in *Dynamic Behavior of Materials, Volume 1: Proceedings of the 2018 Annual Conference on Experimental and Applied Mechanics*, edited by J. Kimberley, L. E. Lamberson, and S. Mates (Springer, Switzerland, 2019), Chap. 50, pp. 269–272.
- [25] J. M. McGlaun, S. L. Thompson, and M. G. Elrick, *Int. J. Impact Eng.* **10**, 351 (1990).
- [26] B. J. Jensen, D. S. Montgomery, A. J. Iverson, C. A. Carlson, B. Clements, and D. A. Fredenburg, in *Shock Phenomena in Granular and Porous Materials*, edited by T. J. Vogler and F. A. Fredenburg (Springer, Cham, Switzerland, 2019), pp. 195–230.
- [27] See Supplemental Material at <http://link.aps.org/supplemental/10.1103/PhysRevMaterials.4.063604> which includes the details of the XRD and PCI experiments, raw XRD images, details of background subtraction and XRD data reduction. It includes Refs. [25,26,29,31].
- [28] N. W. Sinclair, S. J. Turneaure, Y. Wang, K. Zimmerman, and Y. M. Gupta (unpublished).
- [29] T. Sun and K. Fezzaa, *J. Synchrotron Rad.* **23**, 1046 (2016).
- [30] M. G. Gorman, R. Briggs, E. E. McBride, A. Higginbotham, B. Arnold, J. H. Eggert, D. E. Fratanduono, E. Galtier, A. E. Lazicki, H. J. Lee *et al.*, *Phys. Rev. Lett.* **115**, 095701 (2015).
- [31] S. M. Sharma, S. J. Turneaure, J. M. Winey, Y. Li, P. Rigg, A. Schuman, N. Sinclair, Y. Toyoda, X. Wang, N. Weir, J. Zhang, and Y. M. Gupta, *Phys. Rev. Lett.* **123**, 045702 (2019).
- [32] V. Stutzmann, A. Dewaele, J. Bouchet, F. Bottin, and M. Mezouar, *Phys. Rev. B* **92**, 224110 (2015).
- [33] P. Parisiades, F. Cova, and G. Garbarino, *Phys. Rev. B* **100**, 054102 (2019).
- [34] Q. S. Mei, S. C. Wang, H. T. Cong, Z. H. Jin, and K. Lu, *Phys. Rev. B* **70**, 125421 (2004).
- [35] B. L. Davis and M. N. Spilde, *J. Appl. Crystallogr.* **23**, 315 (1990).
- [36] NIST website, <https://www.nist.gov/pml/x-ray-mass-attenuation-coefficients>.
- [37] C. Suryanarayana and M. G. Norton, *X-Ray Diffraction: A Practical Approach*, 1st ed. (Springer, New York, 1998).
- [38] E. A. Owen and R. W. Williams, *Proc. R. Soc. London Ser. A* **188**, 509 (1947).
- [39] T. Taniguchi, K. Kondo, and A. Sawaoka, *J. Appl. Phys.* **61**, 196 (1987).
- [40] P. C. Lysne, *J. Appl. Phys.* **42**, 2152 (1971).
- [41] K.-I. Kondo, S. Soga, A. Sawaoka, and M. Araki, *J. Mater. Sci.* **20**, 1033 (1985).
- [42] B. Lambourn and C. Handley, *AIP Conf. Proc.* **1793**, 120025 (2017).
- [43] R. B. Schwarz, P. Kasiraj, T. Vreeland, and T. J. Ahrens, *Acta Metal.* **32**, 1243 (1984).

- [44] W. H. Gourdin, *J. Appl. Phys.* **55**, 172 (1984).
- [45] G. Kerley, *Int. J. Impact Eng.* **5**, 441 (1987).
- [46] W. Herrmann, *J. Appl. Phys.* **40**, 2490 (1969).
- [47] J. L. Brown, T. J. Vogler, D. E. Grady, W. D. Reinhart, L. C. Chhabildas, and T. F. Thornhill, in *Shock Compression of Condensed Matter - 2007: Proceedings of the Conference of the American Physical Society Topical Group on Shock Compression of Condensed Matter*, edited by M. Elert, M. D. Furnish, R. Chau, N. Holmes, and J. Nguyen, AIP Conf Proc. No. 955 (AIP, New York, 2007), p. 1363.